Check for updates

Thermodynamically Consistent Variational Approach for Modeling Brittle Fracture in Thick Plates by a Hybrid Phase Field Model

P. Raghu
Department of Civil Engineering,
IIT Hyderabad,
Hyderabad, Telangana 502285, India
e-mail: ce16resch01003@iith.ac.in

A. Rajagopal[1]
Department of Civil Engineering,
IIT Hyderabad,
Hyderabad, Telangana 502285, India
e-mail: rajagopal@iith.ac.in

J. N. Reddy
J. Mike Walker '66 Department of Mechanical Engineering,
Texas A&M University,
College Station, TX 77843-3123
e-mail: jnreddy@tamu.edu

In this work, we propose a thermodynamically consistent phase-field model for the brittle fracture analysis of thick plates. A hybrid model, which is fast and accurate, is proposed for the phase-field modeling of fracture in thick plates. Reddy's third-order shear deformation theory (TSDT) has been employed to capture the transverse shear deformation effects in thick plates. Governing equations are derived by seeking the minimization of the free-energy functional. A staggered solution algorithm with arc length control is used to solve the governing equations within the finite element framework. The nucleation and propagation of cracks in the thick plates subjected to uniformly distributed load is presented. The mechanical response corresponding to phase-field models based on both the classical plate theory and TSDT has been compared for the case of thick plates and a significant difference between these two models is observed. Parametric studies have been carried out to illustrate the effects of boundary conditions, shear deformation, and the mesh size.
[DOI: 10.1115/1.4045236]

Keywords: phase field approach, free energy functional, damage mechanics, hybrid model, thick plates, TSDT, finite element formulation, stress analysis

1 Introduction

Modeling fracture in structures plays an important role not only for the efficient and optimal design of structures but also to avoid catastrophic failures. Early works on fracture modeling were mainly attributed to Griffith [1], who first gave an energy-based criterion for the crack extension. The phenomenon where all the deformation tends to concentrate in a narrow region is known as localization. Localization induced by the cracking phenomenon has been proven to be the potential cause of catastrophic failure in structures. Hence, it is important to accurately predict the onset of localization and its effects on the overall response of the structure. Fracture models for the localized failure can be broadly divided into two types: (1) discrete (sharp) crack models and (2) diffuse (smeared) crack models. In discrete crack models, the localization is represented by discrete discontinuities, whereas in diffuse models, it is spread over a certain region using a length scale parameter. Hence, discontinuities are avoided in diffuse models (for more details, see Ref. [2]). Discrete models such as the linear elastic fracture mechanics (LEFM) [1] and cohesive zone model (CZM) which is based on damage mechanics approach [3–5] invoke techniques such as remeshing, interface element technique, and XFEM to resolve the discontinuities. On the other hand, smeared models such as continuum damage models cease to give meaningful results when the material undergoes softening [6,7]. This leads to loss of ellipticity of the mechanical problem. To circumvent this, nonlocal damage models [8] and gradient damage models [9–11] have appeared in the literature.

The phase-field (PF) model was developed as a robust technique to study problems such as micro-structure evolution in solidification and image segmentation. The PF models for *fracture*, which share many features of non-local models, are gaining the attention of researchers in the recent years (see Refs. [12–23]). The term *phase* in the PF models of fracture refers to the two phases of the material during the loading process. One is the undamaged phase and the other is a fully damaged phase. In the PF models of fracture, the evolution of the fracture is directly obtained from the solution of coupled governing equations. The popularity of the regularized models such as the PF model is mainly attributed to their numerical amenability. In contrast to discrete fracture models, there is no need of using sophisticated algorithms to track the fracture surface in the phase-field models. The crack surface can be tracked easily by solving the coupled governing equations which can be derived based on the minimization of the free-energy functional. Francfort and Marigo [24] first proposed the brittle fracture problem as an energy minimization, which can be viewed as the generalization of Griffith's theory of LEFM. The problem of crack nucleation and its propagation is solved in a variational setting. Later, Bourdin et al. [25] regularized the above model by approximating the sharp crack with a diffused crack in a variational framework. This approximation facilitates the numerical solution of the variational formulation. This regularized model invokes the length scale parameter in approximating the crack surface and introduces the gradient of a damage variable. This model draws the motivation from *Ambrosio-Tortorelli regularization* of the *Mumford-Shah functional* in image segmentation [26]. Hence, this model abandons any discontinuities and makes it amicable to the standard finite element method. This model can be reduced to the discrete model in the sense of Γ convergence, when the length scale parameter (l) tends to zero. The counterpart of the Bourdin's regularized variational model [25], which incorporates finite elasticity, can be found in Ref. [27]. In the standard PF models, l is considered as a numerical parameter [28,29]. Since the mesh size must be lesser than the value of l, the results depend on the choice of the l. Recently, Wu et al. [14] presented a length scale insensitive phase field for brittle fracture modeling. This model draws the motivation

[1]Corresponding author.

Contributed by the Applied Mechanics Division of ASME for publication in the Journal of Applied Mechanics. Manuscript received July 8, 2019; final manuscript received October 16, 2019; published online October 18, 2019. Assoc. Editor: Caglar Oskay.

 Copyright © 2019 by ASME

Downloaded from http://asmedigitalcollection.asme.org/appliedmechanics/article-pdf/87/2/021002/6437224/jam_87_2_021002.pdf by Indian Institute of Technology Hyderabad user on 24 November 2022

from Barenblatt's cohesive zone modeling [4], exhibiting Γ convergence.

Though there are many applications of the phase-field method for modeling brittle fracture, only a few applied it for modeling ductile fracture in solids. Ambati et al. [30] proposed a novel model to bring in the effect of ductility in elasto-plastic solids in the quasi-static kinematically linear regime. Miehe et al. [31] presented a coupled PF model of ductile fracture in combination with the gradient plasticity and gradient damage models for the case of large strains. Borden et al. [13] introduced a cubic degradation function unlike a quadratic degradation function found in the literature to model the ductile fracture. Here, they also presented a mechanism for the plastic softening by introducing the yield surface degradation function. This cubic degradation function not only ensures linear elastic-brittle behavior but also prevents nucleation of damage in the regions far from the crack tips. PF models are also employed in a dynamic setting [32,33] and finite strain setting [12,34].

Since the variational type phase-field description does not require any additional criterion to track the crack propagation, the complex crack topologies such as branching and merging can be easily dealt without numerical robustness even in three dimensions. Lee et al. [35] studied the fracture propagation in porous media by demonstrating an efficient algorithm that can save computational time for 3D applications. Borden et al. [36] presented a fourth-order approximation to the crack surface in contrast to the standard second-order approximation of Bourdin et al. [25] and employed it to study the crack propagation in three dimensions. Rajagopal et al. [37] studied the phase separation phenomenon governed by Cahn–Hilliard phase-field equation. Cahn–Hilliard equation is a fourth-order partial differential equation which necessitates the need for piece-wise smooth and globally C^1 continuous shape functions. These are achieved in a natural element framework. Pham et al. [19] developed a three-dimensional finite element code for the phase-field brittle fracture modeling and validated their results with that of experimental results under mixed-mode fracture.

The application of the phase-field method to study the cohesive and adhesive interface fracture is a topic of research in the recent times. Verhoosel and de Borst [38] extended the PF model of brittle fracture to cohesive fracture. Vignollet et al. [39] employed the PF model for a special case of propagative cohesive cracks. This model also shows the insensitivity toward the length scale parameter. Alessi et al. [40] developed a regularized variational formulation for the nucleation of cohesive cracks considering the effect of plasticity. Recently, Rudy et al. [41] presented a phase-field model for cohesive fracture under dynamic loading. Here, they also introduced a linear approximation to the crack surface density and a non-polynomial type degradation function. Hansen-Dörr et al. [42] modeled the adhesive interface failure using the PF method. Here, authors have modified the fracture toughness of the interface material to correct the influence of bulk material on crack propagation along the interface. Paggi and Reinoso [43] developed a framework consisting of the PF model and CZM. This model has been used to solve the problem of crack impinging on an interface. They also utilized this model to predict the crack propagation in a bi-material interface system.

The PF method has also seen limited attention so far toward the application to modeling fracture in composite laminates. Zhang et al. [44] developed a unified phase-field framework based on CZM to model different failure mechanisms in heterogeneous materials such as matrix cracking and debonding of the interface and the interaction between these two. Here, they used two phase fields one for regularizing the material properties of the interface and the other for regularizing the crack. Reinoso et al. [45] compared both the finite fracture mechanics and PF method in predicting the strength of new class of composite materials such as thin ply laminates. Recently, Bleyer and Alessi [46] proposed a novel anisotropic phase-field fracture model by introducing different damage variables for different fracture modes for the case of brittle fracture. This model has been studied to model the fracture phenomenon in fiber-reinforced composites. Dhas et al. [47] presented a PF model for modeling fracture in orthotropic materials such as delamination in composites. This model also embeds traction separation law in order to model the inter-laminar zones.

Some of the very recent research in PF modeling of fracture includes introducing new degradation functions [48], finding alternative approximations to the sharp crack topology especially in the context of dynamic cohesive fracture [41], and developing length scale insensitive PF models [14].

Plates are planar structures that are subjected to loads perpendicular to the plane of the plate. Thick plates find wide applications in Aerospace, Civil, and Mechanical industries. The *classical plate theory* (CPT) is more suitable for the analysis of thin plates where shear deformations will not play a significant role in the mechanical behavior of the plate. For the analysis of thick plates, one must use more realistic theories such as shear deformation theories to correctly capture the mechanical behavior. In this work, we propose a PF model for the brittle fracture analysis of thick plates subjected to different boundary conditions. There is a limited literature available on the application of the phase-field method to model fracture in plates and shells. Amiri et al. [49] first employed this method to study the fracture behavior in thin shells using Kirchoff–Love shell theory. Ambati and De Lorenzis [28] investigated both brittle and ductile fracture in shells employing isogeometric NURBS-based solid shell elements. Kiendl et al. [50] presented a more accurate model for the fracture analysis in thin plates and shells using the Kirchhoff–Love shell model and isogeometric discretization. The application of the PF method for the finite strain analysis of plates and shells can be found in Ref. [51].

The novelty of this work includes proposing a hybrid phase-field model for the fracture modeling in thick plates by invoking a higher-order shear deformation theory such as Reddy's TSDT [52], which requires no shear correction factors and represents the transverse shear stresses quadratically through the plate thickness. The hybrid model proposed here draws the motivation from Ref. [53], which was originally proposed for plane problems. In the hybrid model, the effect of damage is applied to the entire strain energy density when defining the Cauchy stress, that is without considering a tension–compression split, whereas the history parameter driving the damage evolution depends only on the tensile part of the strain energy density. More details on this model are presented in Sec. 4.

The outline of the paper is as follows. In Sec. 2, we present both the sharp and phase-field crack topologies and the phase regularized crack functional. In Sec. 3, we show the variational approach to the brittle fracture model considering various existing formulations. In Sec. 4, we present the proposed phase-field formulation along with the plate kinematics. In Sec. 5, we derive the finite element model for the governing equations. In Sec. 6, we present the implementation aspects such as staggered algorithm and arc length method. Section 7 presents different numerical examples to show the effectiveness of the present model. Finally Sec. 8 presents the conclusions drawn from the work.

2 Phase-Field Description of Fracture

In this section, we introduce the phase-field method in the context of fracture modeling. The PF method serves an approximation to the discrete fracture models in the sense that the sharp crack surface is approximated by a diffused crack surface.

2.1 Representation of Crack Topology. Phase-field method avoids the discontinuities in displacement by ensuring a smooth transition between the fully damaged and undamaged material. The variable introduced to represent these two phases and the transition is called crack phase field or order parameter (ϕ). A crack of width zero is spread over a region of radius equal to the length scale parameter l. For one-dimensional case, the order parameter can be represented in the following way.

Downloaded from http://asmedigitalcollection.asme.org/appliedmechanics/article-pdf/87/2/021002/6437224/jam_87_2_021002.pdf by Indian Institute of Technology Hyderabad user on 24 November 2022

Assume a crack located at $x=0$ with fully broken crack surface Γ in an infinite bar, as shown in Fig. 1(*a*), the order parameter for the sharp crack topology can be written as

$$\phi(x) = \begin{cases} 1, & x = 0 \\ 0, & \text{otherwise} \end{cases} \tag{1}$$

For the case of the diffused crack model as shown in Fig. 1(*b*), the order parameter can be written as

$$\phi(x) = e^{-|x|/l}, \quad -\infty < x < +\infty \tag{2}$$

The above approximation of the diffused crack model satisfies the following boundary conditions:

$$\phi(0) = 1 \quad \text{and} \quad \phi(\pm\infty) = 0 \tag{3}$$

It is observed that, Eq. (2) is the solution of the following homogeneous differential equation:

$$\phi(x) - l^2 \frac{d^2}{dx^2}(\phi(x)) = 0 \tag{4}$$

subjected to the boundary conditions (3). This differential equation (4) is the Euler equation of the following variational principle:

$$\phi = Arg\left\{ \underset{\phi\in\zeta}{Inf} \; F(\phi) \right\} \tag{5}$$

where $\zeta = \{\phi | \phi(0) = 1, \phi(\pm\infty) = 0\}$, with the functional

$$F(\phi) = \frac{1}{2}\int_{\Omega} \left(\phi^2 + l^2\phi'^2\right) d\Omega \tag{6}$$

which is the Galerkin type weak form of Eq. (4). The resultant functional for the approximation given in Eq. (2) together with $d\Omega = \Gamma\, dx$ gives the following identification:

$$F\left(\phi = e^{-|x|/l}\right) = l\Gamma \tag{7}$$

Consequently, we can introduce the functional of the form

$$\Gamma_l(\phi) := \frac{1}{l}F(\phi) = \frac{1}{2l}\int_{\Omega} \left(\phi^2 + l^2\phi'^2\right) d\Omega \tag{8}$$

where Γ is the crack surface in the sharp crack topology [25,29]. Equation (8) approximates the surface integral as the volume integral. This regularized functional Γ_l can be viewed as the crack surface itself which serves as the main ingredient of the phase-field model.

Figure 2 represents both the sharp crack topology and phase-field regularized crack topology. The crack phase field is approximated as a finite band as shown in Fig. 2(*b*). $\phi = 0$ corresponds to the undamaged state and $\phi = 1$ represents the fully damaged state.

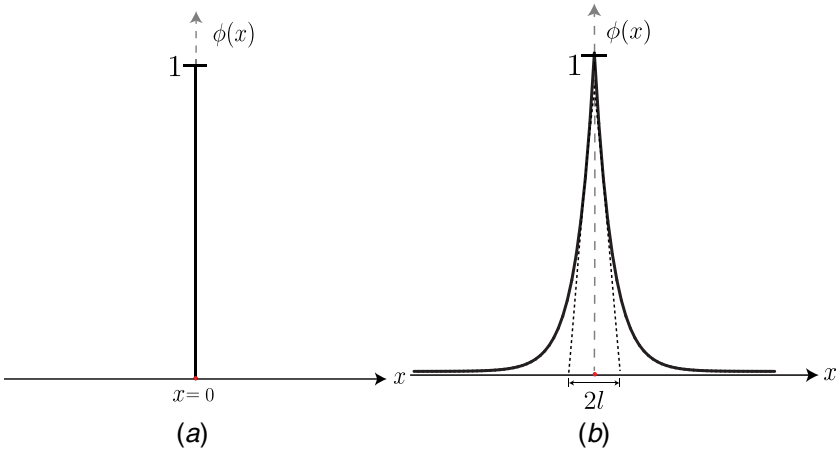

Fig. 1 (*a*) Sharp crack model and (*b*) diffused crack model

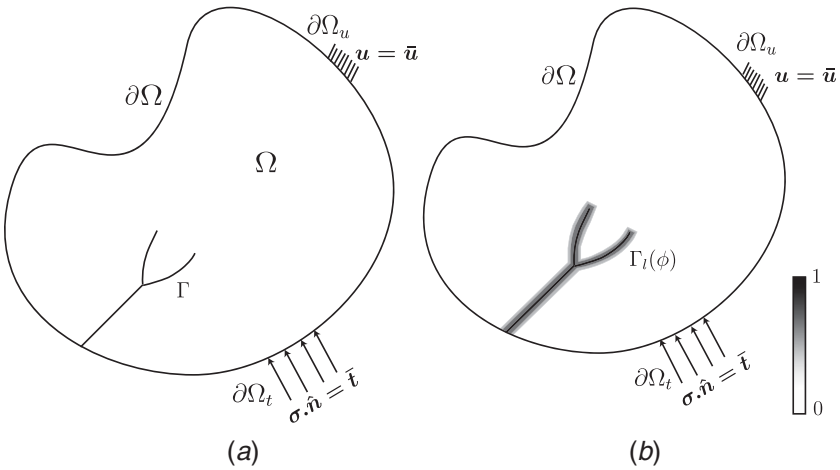

Fig. 2 2D representation of (*a*) sharp crack topology and (*b*) phase-field crack topology

Downloaded from http://asmedigitalcollection.asme.org/appliedmechanics/article-pdf/87/2/021002/6437224/jam_87_2_021002.pdf by Indian Institute of Technology Hyderabad user on 24 November 2022

In two dimensions, the crack surface functional can be written as

$$\Gamma_l = \int_\Omega \gamma(\phi, \nabla\phi)\, d\Omega \tag{9}$$

where γ is the crack surface density, which can be expressed in terms of crack phase field and its gradient within the localization region as

$$\gamma(\phi, \nabla\phi) = \frac{\phi^2}{2l} + \frac{l}{2}|\nabla\phi|^2 \tag{10}$$

3 Variational Approach to Brittle Fracture

In this section, we present a variational approach to the fracture model. We also present how the minimization of the free-energy functional leads to the governing equations that can be solved in a finite element framework.

Cracking is a dissipative process. The solution for the crack extension is governed by the minimization of the following free-energy functional

$$E = \psi_v + \psi_s \tag{11}$$

where ψ_v is the elastic strain energy integrated over the volume and ψ_s is the surface energy integrated over the surface. It can be further written as

$$E = \int_\Omega \psi_e\, d\Omega + G_c \int_\Gamma d\Gamma \tag{12}$$

where ψ_e is the elastic strain energy density and G_c is the material parameter known as Griffith's critical energy release rate. Following thermodynamic principles, the free-energy functional leads to the following conditions:

$$\left(\mathcal{G} - G_c\right)\dot{\Gamma} = 0 \tag{13}$$

which is the equation of the conservation of energy. $\mathcal{G}$ is the energy release rate $\mathcal{G} = -(\partial\psi_s/\partial\Gamma)$ and the Kuhn–Tucker loading/unloading conditions read as

$$\dot{\Gamma} \geq 0, \quad \mathcal{G} - G_c \leq 0, \quad (\mathcal{G} - G_c)\dot{\Gamma} = 0 \tag{14}$$

Equations (14) and (13) are equivalent to the Griffith's theory.

3.1 Regularized Model. The variational approach for brittle fracture (12) model proposed by Francfort and Marigo [24] is equivalent to the sharp crack model for which robust numerical strategies have to be used to find the solution. To circumvent this, Bourdin et al. [25] proposed a regularized variational fracture model. In this model, the sharp crack is approximated as a diffused crack invoking a length scale parameter as shown in Eqs. (9) and (10).

The free-energy functional with a regularized crack surface density can now be written as,

$$E_l = \int_\Omega g(\phi)\psi_e\, d\Omega + \int_\Omega \psi_\phi\, d\Omega \tag{15}$$

where

$$\begin{aligned}\int_\Omega \psi_\phi(\phi, \nabla\phi)\, d\Omega &= \int_A \int_{-(h/2)}^{h/2} \psi_\phi\, dA\, dz \\ &= \int_A hG_c\left\{\frac{\phi^2}{2l} + \frac{l}{2}|\nabla\phi|^2\right\} dA\end{aligned} \tag{16}$$

where the damage parameter ϕ is assumed to be invariant thorough the thickness; $g(\phi)$ is called the degradation function that models the degradation of elastic stiffness as the damage progresses in the bulk material. This function also couples the elastic equilibrium equation with the evolution equation. The degradation function has to satisfy the following conditions to ensure the thermodynamically consistent variational formulation

- $g(0) = 1 \Rightarrow$ no degradation of elastic stiffness when the material is intact.
- $g(0) = 1 \Rightarrow$ full degradation of elastic stiffness when the material is fully damaged.
- Thermodynamic conjugate force is defined as $F = -g'(\phi)\psi_e$. This takes the value zero when the material is fully damaged. Therefore, $g'(1) = 0$.

The function satisfying the above properties can be taken as

$$g(\phi) = (1 - \beta)(1 - \phi)^2 + \beta \tag{17}$$

where β is a very small positive scalar value ($\ll 1$) introduced to avoid the ill conditioning of the stiffness matrix when $\phi = 1$. The variation of $g(\phi)$ with ϕ is shown in Fig. 3.

3.1.1 Models With Tension-Compression Split. The model shown in Sec. 3.1 does not differentiate the fracture response in tension and compression, hence results in physically unrealistic crack patterns. To avoid such discrepancy, Miehe et al. [54] modified the Bourdin's [25] regularized formulation by introducing the additive decomposition of the elastic strain energy into tensile and compressive parts. The degradation is applied only on the tensile part of ψ_e.

According to Miehe et al. [54], the first term in the Eq. (15) is replaced by the following expression:

$$\psi_e = \psi_e^+ + \psi_e^- \tag{18}$$

where

$$\psi_e^\pm = \frac{1}{2}\lambda\langle tr(\boldsymbol{\varepsilon})\rangle_\pm^2 + \mu tr(\boldsymbol{\varepsilon}_\pm^2) \tag{19}$$

The above split is based on the spectral decomposition of the strain tensor; $\boldsymbol{\varepsilon} = \sum_{i=1}^3 \langle\varepsilon_i\rangle\, \boldsymbol{n}_i \otimes \boldsymbol{n}_i$, $\boldsymbol{\varepsilon}_\pm = \sum_{i=1}^3 \langle\varepsilon_i\rangle_\pm\, \boldsymbol{n}_i \otimes \boldsymbol{n}_i$, where ε_i and $\boldsymbol{n}_i$ are the principal strains and their directions, respectively; λ and μ are Lamés parameters and $\langle\alpha\rangle_\pm = \frac{1}{2}(\alpha \pm |\alpha|)$.

Therefore, the regularized free-energy functional with the tension-compression (T-C) split of the strain energy can be written as

$$E_l = \int_\Omega \left(g(\phi)\psi_e^+ + \psi^-\right) d\Omega + \int_\Omega \psi_\phi\, d\Omega \tag{20}$$

3.1.2 Hybrid Model. The above formulation makes the elastic equilibrium equation nonlinear because of the split, hence the computational time to solve the governing equations increases.

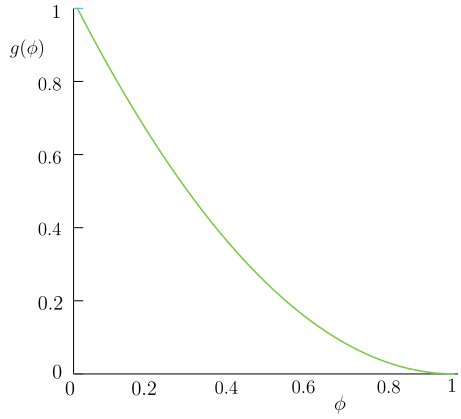

Fig. 3 Variation of $g(\phi)$ with ϕ

Downloaded from http://asmedigitalcollection.asme.org/appliedmechanics/article-pdf/87/2/021002/6437224/jam_87_2_021002.pdf by Indian Institute of Technology Hyderabad user on 24 November 2022

To avoid this, we propose a hybrid formulation that greatly reduces the computational time. In the hybrid model, no split is applied on ψ_e in the elastic equilibrium equation whereas the positive part of the history variable based on ψ_e^+ is supplied to the evolution equation. Hence, the linearity of the elastic equilibrium equation is preserved. The hybrid formulation for the analysis of plates is presented in Sec. 4.

4 Proposed Formulation

In this section, we develop the phase-field formulation for brittle fracture analysis in thick plates. This formulation can accurately predict the response of thick plates as we aim to use a higher order shear deformation theory proposed by Reddy [52].

4.1 Plate Kinematics of Reddy's TSDT [52]. The transverse shear deformation plays a major role in the overall behavior of thick plates. The classical plate theory (*Kirchhoff–Love*) does not include shear deformation and thus not suitable for the analysis of thick plates. On the other hand, the first-order shear deformation theory requires shear correction factor since it predicts the constant variation of transverse shear stress through the thickness.

The third-order shear deformation theory of Reddy [52] avoids any shear correction factors as it correctly predicts the quadratic variation of transverse shear stress through the thickness by expanding the in-plane displacements up to the third-degree of the thickness coordinate. The total displacement of a point 'a' as shown in Fig. 4 can be written as

$$\begin{aligned} u(x,y,z) &= u_0(x,y) + z\phi_x - \frac{4z^3}{3h^2}\left(\phi_x + \frac{\partial w_0}{\partial x}\right) \\ v(x,y,z) &= v_0(x,y) + z\phi_y - \frac{4z^3}{3h^2}\left(\phi_y + \frac{\partial w_0}{\partial y}\right) \\ w(x,y,z) &= w_0(x,y) \end{aligned} \tag{21}$$

where (u_0, v_0, w_0) are in-plane displacements of a point on the mid-plane (i.e., $z=0$). ϕ_x and ϕ_y denote the rotations of a transverse normal line at the mid-plane ($\phi_x = \partial u/\partial z$ and $\phi_y = \partial v/\partial z$). The total thickness of the laminate is denoted by h. The cubic variation of the displacement field with the thickness coordinate allows a parabolic variation of the transverse shear strains and shear stresses hence avoids the need for shear correction factors.

4.2 Strain–Displacement Relations. The strain components for the linear strains of third-order shear deformation theory are

$$\begin{Bmatrix} \varepsilon_{xx} \\ \varepsilon_{yy} \\ \gamma_{xy} \end{Bmatrix} = \begin{Bmatrix} \varepsilon_{xx}^{(0)} \\ \varepsilon_{yy}^{(0)} \\ \gamma_{xy}^{(0)} \end{Bmatrix} + z\begin{Bmatrix} \varepsilon_{xx}^{(1)} \\ \varepsilon_{yy}^{(1)} \\ \gamma_{xy}^{(1)} \end{Bmatrix} + z^3\begin{Bmatrix} \varepsilon_{xx}^{(3)} \\ \varepsilon_{yy}^{(3)} \\ \gamma_{xy}^{(3)} \end{Bmatrix} \tag{22}$$

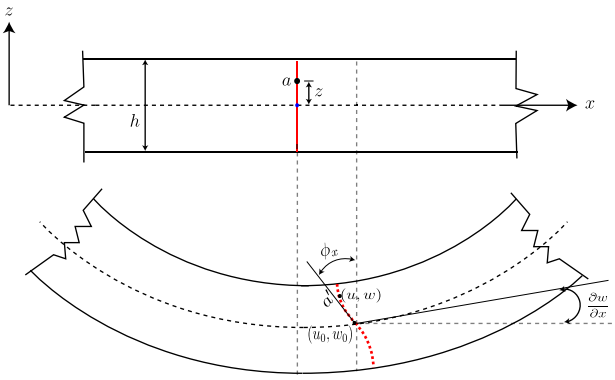

Fig. 4 Deformation of transverse normal according to TSDT

$$\begin{Bmatrix} \gamma_{yz} \\ \gamma_{xz} \end{Bmatrix} = \begin{Bmatrix} \gamma_{yz}^{(0)} \\ \gamma_{xz}^{(0)} \end{Bmatrix} + z^2\begin{Bmatrix} \gamma_{yz}^{(2)} \\ \gamma_{xz}^{(2)} \end{Bmatrix} \tag{23}$$

where

$$\begin{Bmatrix} \varepsilon_{xx}^{(0)} \\ \varepsilon_{yy}^{(0)} \\ \gamma_{xy}^{(0)} \end{Bmatrix} = \begin{Bmatrix} \dfrac{\partial u_0}{\partial x} \\ \dfrac{\partial v_0}{\partial y} \\ \dfrac{\partial u_0}{\partial y} + \dfrac{\partial v_0}{\partial x} \end{Bmatrix}, \quad \begin{Bmatrix} \varepsilon_{xx}^{(1)} \\ \varepsilon_{yy}^{(1)} \\ \gamma_{xy}^{(1)} \end{Bmatrix} = \begin{Bmatrix} \dfrac{\partial \phi_x}{\partial x} \\ \dfrac{\partial \phi_y}{\partial y} \\ \dfrac{\partial \phi_x}{\partial y} + \dfrac{\partial \phi_y}{\partial x} \end{Bmatrix} \tag{24}$$

$$\begin{Bmatrix} \varepsilon_{xx}^{(3)} \\ \varepsilon_{yy}^{(3)} \\ \gamma_{xy}^{(3)} \end{Bmatrix} = -c_1\begin{Bmatrix} \dfrac{\partial \phi_x}{\partial x} + \dfrac{\partial^2 w_0}{\partial x^2} \\ \dfrac{\partial \phi_y}{\partial y} + \dfrac{\partial^2 w_0}{\partial y^2} \\ \dfrac{\partial \phi_x}{\partial y} + \dfrac{\partial \phi_y}{\partial x} + 2\dfrac{\partial^2 w_0}{\partial x \partial y} \end{Bmatrix} \tag{25}$$

$$\begin{Bmatrix} \gamma_{yz}^{(0)} \\ \gamma_{xz}^{(0)} \end{Bmatrix} = \begin{Bmatrix} \phi_y + \dfrac{\partial w_0}{\partial y} \\ \phi_x + \dfrac{\partial w_0}{\partial x} \end{Bmatrix}, \quad \begin{Bmatrix} \gamma_{yz}^{(2)} \\ \gamma_{xz}^{(2)} \end{Bmatrix} = -c_2\begin{Bmatrix} \phi_y + \dfrac{\partial w_0}{\partial y} \\ \phi_x + \dfrac{\partial w_0}{\partial x} \end{Bmatrix} \tag{26}$$

As can be seen in Eq. (23), the transverse shear strains vary quadratically through the thickness.

4.3 Hybrid Phase Field Model of Brittle Fracture for Plates. The plate theories dimensionally reduce the continuum formulation to 2D using the mid surface and the thickness. The displacements are evaluated on the mid surface of the plate and the thickness-wise variations of stresses and strains can be calculated based on the strain–displacement and stress–strain relations. Therefore, the free-energy functional can be written as

$$E_l = \int_A \left(g(\phi)\psi + hG_c\left\{\frac{\phi^2}{2l} + \frac{l}{2}|\nabla\phi|^2\right\}\right) dA \tag{27}$$

where ψ is the elastic strain energy density obtained after integrating through the thickness. The thickness-wise integration is done using the Simpson's rule.

$$\psi = \int_{-(h/2)}^{h/2} \psi_e(z)\, dz \tag{28}$$

One can derive the governing equations by seeking the minimization of the free-energy functional (27). This is achieved by invoking the Euler equation. For a given functional J of the form,

$$J = \int_\Omega L(\alpha, \nabla\alpha)\, d\Omega \tag{29}$$

the Euler equation is written as

$$\frac{\delta J}{\delta \alpha} = \frac{\partial L}{\partial \alpha} - \nabla \cdot \frac{\partial L}{\partial \nabla \alpha} = 0 \tag{30}$$

Therefore, the functional derivative of the free-energy functional w.r.t to displacement and damage variable is made zero, which results in the following governing equations:

$$\frac{\delta E_l}{\delta \boldsymbol{u}} = 0 \Rightarrow \nabla \cdot \boldsymbol{\sigma} = 0 \tag{31a}$$

$$\frac{\delta E_l}{\delta \phi} = 0 \Rightarrow 2(1-\beta)(1-\phi)\mathcal{H}^+ = \frac{hG_c}{l}\left(\phi - l^2\nabla\cdot\nabla\phi\right) \tag{31b}$$

Downloaded from http://asmedigitalcollection.asme.org/appliedmechanics/article-pdf/87/2/021002/6437224/jam_87_2_021002.pdf by Indian Institute of Technology Hyderabad user on 24 November 2022

with the boundary conditions

$$\boldsymbol{u} = \bar{\boldsymbol{u}} \quad \text{on } \partial\Omega_u \tag{32a}$$

$$\boldsymbol{\sigma} \cdot \hat{\boldsymbol{n}} = \bar{\boldsymbol{t}} \quad \text{on } \partial\Omega_t \tag{32b}$$

$$\nabla\phi \cdot \hat{\boldsymbol{n}} = 0 \quad \text{on } \partial\Omega \tag{32c}$$

where $\boldsymbol{\sigma}(\boldsymbol{u}, \phi) = g(\phi)(\partial\psi_e/\partial\varepsilon)$, $\mathcal{H}^+ = \max_{t\in[0,\,\tau]} \psi^+(\boldsymbol{\varepsilon}, t)$, $\bar{\boldsymbol{t}}$ is the traction force vector, and $\hat{\boldsymbol{n}}$ is the unit outward normal vector to the boundary. $\partial\Omega_u$ and $\partial\Omega_t$ are the Dirichlet and Neumann boundaries, respectively, with $\partial\Omega_u \cup \partial\Omega_t = \partial\Omega$ and $\partial\Omega_u \cap \partial\Omega_t = \emptyset$. The history parameter $\mathcal{H}^+$ is equal to the maximum value of accumulated ψ^+ within the loading history. This can be viewed as the driving force for the phase-field evolution. This history variable not only ensures the crack irreversibility condition but also facilitates the decoupling of two governing equations. This history field satisfies the loading and unloading conditions defined as

$$\left(\mathcal{H}^+ - \psi^+\right) \geq 0, \quad \dot{\mathcal{H}}^+ \geq 0, \quad \dot{\mathcal{H}}^+\left(\psi^+ - \mathcal{H}^+\right) = 0 \tag{33}$$

The positive energy calculation is done as follows:

$$\psi_e^+ = \frac{1}{2}\lambda\left(\langle tr(\boldsymbol{\varepsilon})\rangle^+\right)^2 + \mu tr\left(\boldsymbol{\varepsilon}^+\right)^2 - \frac{\lambda^2}{2(\lambda+2\mu)}\left(\langle tr(\boldsymbol{\varepsilon})\rangle^+\right)^2 + \frac{1}{2}\mu(\gamma_{xz}^2 + \gamma_{yz}^2) \tag{34}$$

The above formula draws the motivation from the works of Kiendl et al. [50] who derived it without accounting for transverse shear strains.

5 Galerkin Finite Element Formulation

In this section, we develop the finite element formulation for the governing equation (31*b*). The weak form and the discretized weak form for the evolution equation are presented. The weak forms for the evolution equation (31*b*) can be obtained as follows:

$$\int_A \delta w\left(\frac{hG_c}{l}(\phi - l^2\triangle\phi) - 2(1-\beta)(1-\phi)\mathcal{H}^+\right) dA = 0 \tag{35}$$

where δw is the weighting function. The use of divergence theorem further leads to the following:

$$\int_A \left\{\delta w \frac{hG_c}{l}\phi + hG_c l\,\nabla\phi \cdot \nabla\delta w - 2(1-\beta)(1-\phi)\mathcal{H}^+\delta w\right\} dA - \oint_{\partial\Omega} hG_c l\,\delta w \nabla\phi \cdot \hat{n}\, dS = 0 \tag{36}$$

5.1 Finite Element Approximation. From the above weak form, it can be deduced that the primary variable ϕ can be approximated using Lagrangian interpolation functions in a given finite element:

$$\phi = \sum_{j=1}^{n} \phi_j N_j \tag{37}$$

where n is the number of degree-of-freedom (DOF) in a given element and N_j are the Lagrange interpolation functions. Substituting the above approximation, i.e., Eq. (37) in the weak form, i.e., Eq. (36), we can arrive at the following discretized form of the weak form:

$$[\boldsymbol{K}]\{\phi\} = \boldsymbol{f} \tag{38}$$

The stiffness matrix and force vector are given as

$$K_{ij}^{\phi\phi} = \int_A \left\{\frac{hG_c}{l}N_i N_j + hG_c l\left(\frac{\partial N_i}{\partial x}\frac{\partial N_j}{\partial x} + \frac{\partial N_i}{\partial y}\frac{\partial N_j}{\partial y}\right) + 2(1-\beta)\mathcal{H}^+ N_i N_j\right\} dx\,dy \tag{39}$$

$$f_i^{\phi} = \int_A 2(1-\beta)\mathcal{H}^+ N_i\, dx\, dy \tag{40}$$

The discretized weak form of the elastic equilibrium equation (see Ref. [55] for more details) using TSDT suggests that the finite element should possess eight degree-of-freedom at each node. These DOFs are approximated in the following manner:

$$u(x, y) \approx \sum_{j=1}^{m} U_j N_j^{(1)}(x, y) \tag{41}$$

$$v(x, y) \approx \sum_{j=1}^{m} V_j N_j^{(1)}(x, y) \tag{42}$$

$$w(x, y) \approx \sum_{j=1}^{n} \bar{\Delta}_j \varphi_j(x, y) \tag{43}$$

$$\phi_x(x, y) \approx \sum_{j=1}^{n} \mathcal{X}_j N_j^{(2)}(x, y) \tag{44}$$

$$\phi_y(x, y) \approx \sum_{j=1}^{n} \mathcal{Y}_j N_j^{(2)}(x, y) \tag{45}$$

where u and v are inplane displacements, w is the transverse deflection that also includes the rotations ($\partial w/\partial x$, $\partial w/\partial y$, $\partial^2 w/\partial x\partial y$) and ϕ_x, ϕ_y are the shear deformations. $N^{(\alpha)}$ represents the linear Lagrange interpolation function and φ represents the Hermite interpolation (which are C^1 continuous) function. In this work, $N^{(1)}$ is taken equal to $N^{(2)}$.

6 Numerical Implementation

This section presents the numerical treatment of the governing equations. The governing equations in the phase-field approach can be solved either in a monolithic manner or in a staggered manner. In the monolithic approach, both the displacement and phase field are solved concurrently, whereas in the staggered approach, they are solved alternatively. The following staggered algorithm is adopted in this work. This algorithm renders the equations to solve in a rather straight forward way. In order to capture the softening behavior, arc length control has been adopted. Below we present the staggered algorithm to solve the phase-field fracture (The notation n and i are used to represent the load steps and iterations, respectively.).

(1) Loop on load steps ($n = 1$ to $n_{\max}$)
(2) Loop on iterations ($i = 1$ to $i_{\max}$)
(3) Freeze ϕ and solve for $\boldsymbol{u}$ using Eq. (31a)
(4) Using the calculated $\boldsymbol{u}$ obtain ϕ from Eq. (38)
(5) If error $\leq$ tolerance, go to step 1 else, go to step 2

6.1 Arc Length Method. Arc length method is a powerful incremental iterative solution technique to trace the equilibrium path. The idea of arc length to trace the subsequent equilibrium point was first given by Riks [56] for the solution of snapping and buckling problems. Riks proposed this solution technique based on the constant arc length. Later, Crisfield [57] proposed the arc length method based on the cylindrical arc length. This method involves choosing one root of the second-order equation

Downloaded from http://asmedigitalcollection.asme.org/appliedmechanics/article-pdf/87/2/021002/6437224/jam_87_2_021002.pdf by Indian Institute of Technology Hyderabad user on 24 November 2022

to find the increment or decrement in the load. This causes problems in cases where the equation does not have a real root. To avoid this, we use the combination of the Crisfield and Ramm arc length method. The algorithm for the same is presented below.

Let the nonlinear equation to be solved be given by

$$[K(\boldsymbol{u})]\{\boldsymbol{u}\} = \{\boldsymbol{F}\} \tag{46}$$

The linearized version of above equation using Newton Raphson iteration can be written as

$$[T(\boldsymbol{u}_{i-1})]\{\Delta\boldsymbol{u}\} = \{\boldsymbol{R}(u_{i-1})\} \tag{47}$$

where T is the tangent stiffness matrix defined as $[T] = -[\partial \boldsymbol{R}/\partial \boldsymbol{u}]$ and i represents the iteration number. The following quantities are used in the arc length algorithm.

$$\{\Delta\boldsymbol{u}_{R_i}\} = [T_i]^{-1}\{\boldsymbol{R}_i\} \tag{48}$$

$$\{\Delta\boldsymbol{u}_{F_i}\} = [T_i]^{-1}\{\boldsymbol{F}\} \tag{49}$$

where

$$\boldsymbol{R}(\boldsymbol{u}_{i-1}) = \lambda\{\boldsymbol{F}\} - [K(\boldsymbol{u}_{i-1})]\{\boldsymbol{u}_{i-1}\} \tag{50}$$

and $\boldsymbol{F}$ is the total load to be applied and λ is the load increment factor.

The increment in the displacement is calculated as follows:

$$\{\Delta\boldsymbol{u}_i^n\} = \{\Delta\boldsymbol{u}_{R_i}^n\} + \delta\lambda_i^n\{\Delta\boldsymbol{u}_{F_i}^n\} \tag{51}$$

The load increment factor λ is updated in the following manner:

$$\lambda_{i+1}^n = \lambda_i^n + \Delta\lambda_{i+1}^n \tag{52}$$

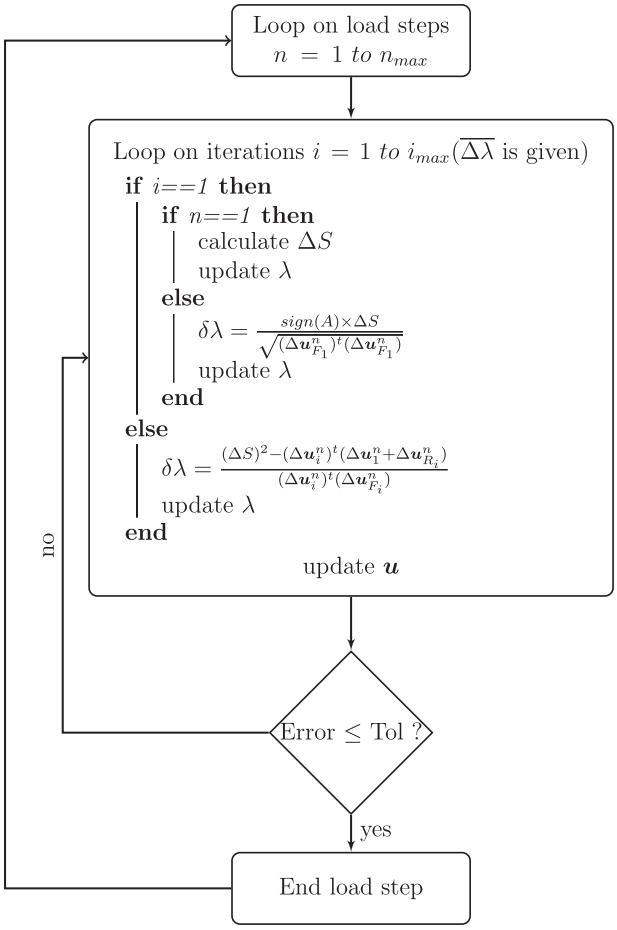

Fig. 5 Flowchart of Crisfield–Ramm arc length algorithm

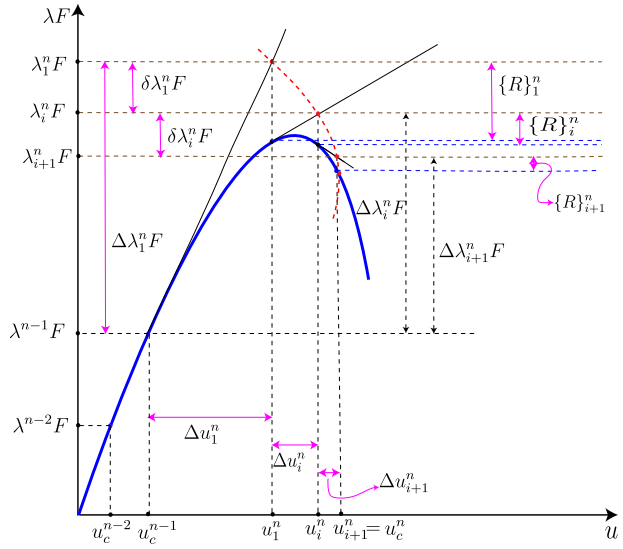

Fig. 6 Graphical interpretation of the Arc length method

where

$$\Delta\lambda_{i+1}^n = \Delta\lambda_i^n + \delta\lambda_i^n \tag{53}$$

For the first iteration, the value of $\delta\lambda_i^n$ (i.e., $\delta\lambda_1^n$) is zero. The flowchart and the graphical interpretation of arc length method are presented in Figs. 5 and 6, respectively.

u_c^n represents the converged displacement in the nth load step. The length of the arc length is calculated as follows:

$$\Delta S = \Delta\lambda\sqrt{(\Delta\boldsymbol{u}_{F_i}^n)^t(\Delta\boldsymbol{u}_{F_i}^n)} \tag{54}$$

Other quantities used in the arc length method are as follows:

$$A = (\boldsymbol{u}_c^{n-1} - \boldsymbol{u}_c^{n-2})^t\,(\Delta\boldsymbol{u}_{F_1}^n) \tag{55}$$

$$sign(A) = \frac{|A|}{A} \tag{56}$$

7 Numerical Examples

In this section, we present numerical examples to study the damage evolution in thick and thin plates subjected to uniformly distributed load. The difference in the PF models of the classical plate theory and TSDT has been brought out. Different boundary conditions as shown in Figs. 7 and 8 are applied. In SS-1 boundary conditions, the following quantities are constrained on the edges parallel to the x-axis. The inplane displacement along the x-axis,

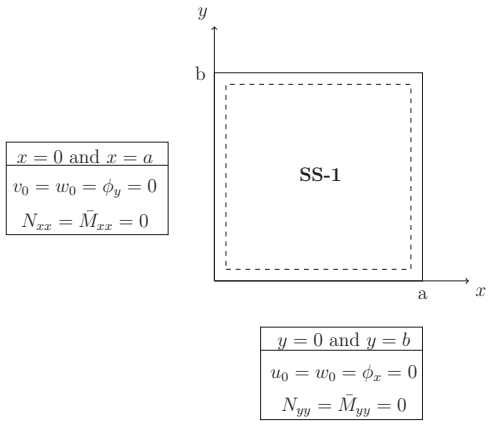

Fig. 7 SS-1 boundary conditions

Downloaded from http://asmedigitalcollection.asme.org/appliedmechanics/article-pdf/87/2/021002/6437224/jam_87_2_021002.pdf by Indian Institute of Technology Hyderabad user on 24 November 2022

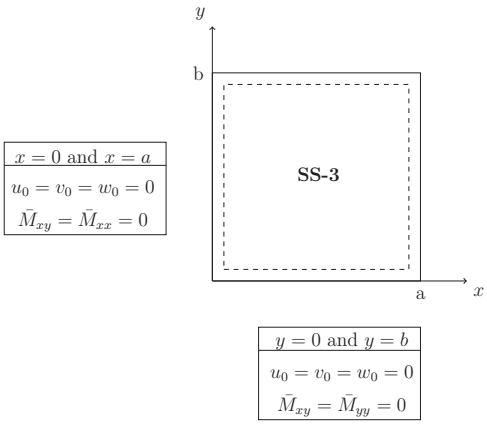

Fig. 8 SS-3 boundary conditions

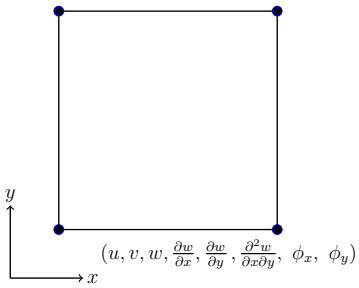

Fig. 9 Four-noded rectangular element

transverse deflection, shear deformation (rotation along the y-axis), N_{yy} and $\bar{M}_{xx}$. Whereas on the edges parallel to y-axis, the inplane displacement along the y-axis, transverse deflection, shear deformation (rotation along the x-axis), N_{xx} and $\bar{M}_{yy}$ are constrained. In SS-3 boundary conditions, on all the edges the

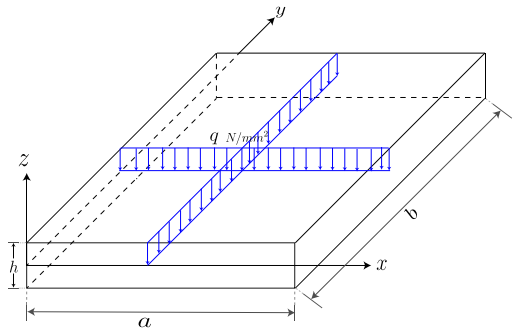

Fig. 10 Plate subjected to uniformly distributed load

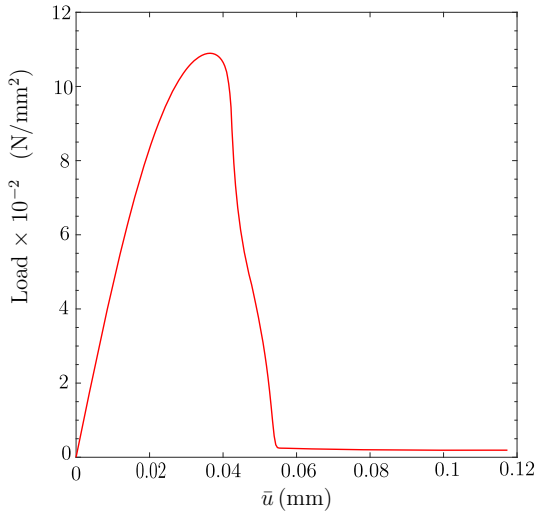

Fig. 12 Load versus deflection diagram

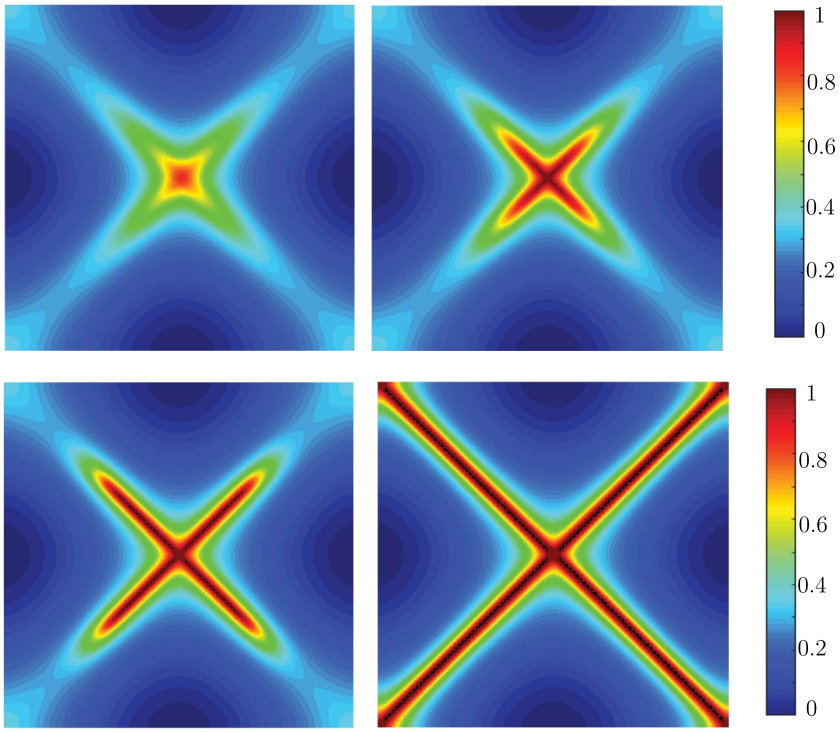

Fig. 11 Evolution of damage at different stages of loading in thin plate (full plate is visualized) subjected to SS-1 boundary conditions

Downloaded from http://asmedigitalcollection.asme.org/appliedmechanics/article-pdf/87/2/021002/6437224/jam_87_2_021002.pdf by Indian Institute of Technology Hyderabad user on 24 November 2022

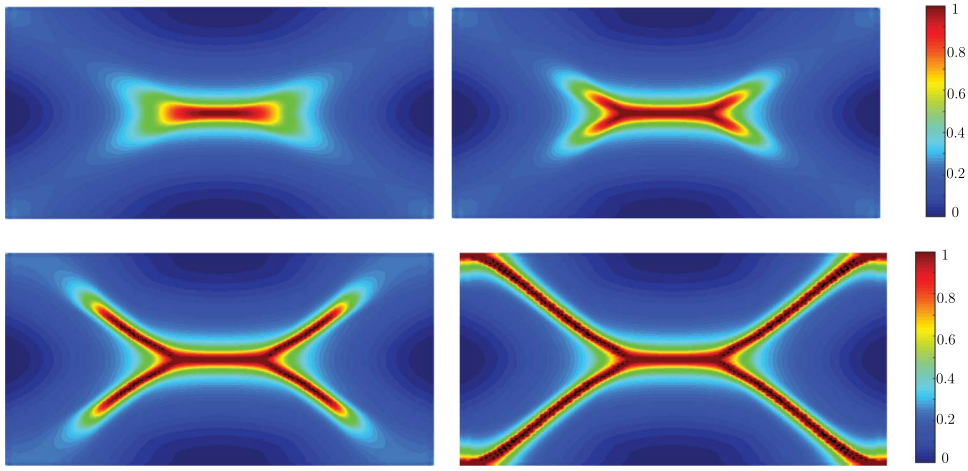

Fig. 13 Evolution of damage at different stages of loading in a thin rectangular plate subjected to SS-3 boundary conditions

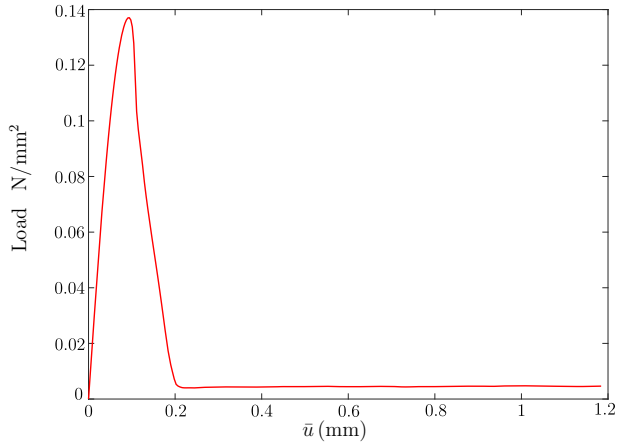

Fig. 14 Load versus deflection diagram

inplane displacement along the x- and y-axes, transverse deflection, and $\bar{M}_{xy}$ are constrained and $\bar{M}_{yy}$ and $\bar{M}_{xx}$ are constrained on the edges parallel to x- and y-axes, respectively.

Where $\bar{M}_{\alpha\beta}$ and $N_{\alpha\beta}$ represent the stress resultants defined as

$$\begin{Bmatrix} N_{\alpha\beta} \\ M_{\alpha\beta} \\ P_{\alpha\beta} \end{Bmatrix} = \int_{-(h/2)}^{h/2} \sigma_{\alpha\beta} \begin{Bmatrix} 1 \\ z \\ z^3 \end{Bmatrix} dz \tag{57}$$

$\bar{M}_{\alpha\beta} = M_{\alpha\beta} - c_1 P_{\alpha\beta}$, $c_1 = 4/3h^2$. For more details, see Ref. [55].

Only the quarter plate is modeled wherever symmetry is present and the results are assembled to see the full plate visualization. Four-noded conforming rectangular finite elements are used to model the geometry of the plate. Each node of the element has 8 degree-of-freedom (along with the damage variable) as shown in Fig. 9. In all the examples, the plate is subjected to uniformly distributed load as shown in Fig. 10. The selective integration scheme is used to evaluate the stiffness matrix.

The following material properties are used: $E = 190 \times 10^3$ Mpa, $\nu = 0.29$, $G_c = 0.295$ N/mm. The normalized deflection is calculated as follows: $\bar{u} = \sqrt{(\boldsymbol{u}^t \times \boldsymbol{u})/u_n}$, where u_n is the total number of displacements. In all the simulations, the phase-field parameter ϕ is taken as zero in the first step of the analysis and a tolerance value of 10^{-3} is used.

7.1 Example 1: Thin Square Plate Analysis. In this example, a thin square plate of dimensions 2 mm × 2 mm and a/h equal to 100 is considered. SS-1 boundary conditions as shown in Fig. 7 are considered. A uniform mesh of 10,000 elements is considered, and the value of the length scale is fixed as 0.04 mm. A total load of 15 N is applied with an initial λ value in the arc length method equal to 55×10^{-6}. The number of load steps used is 320.

Figure 11 shows the nucleation and propagation of the damage in the plate. The full plate has been assembled for visualization. It is observed that the damage initiates at the center of the plate as the bending moment is maximum at the center and propagates toward the corners of the plate. Similar trends are observed by Kiendl et al. [50] whose model is based on the classical plate theory. Figure 12 shows the load versus the normalized deflection. The

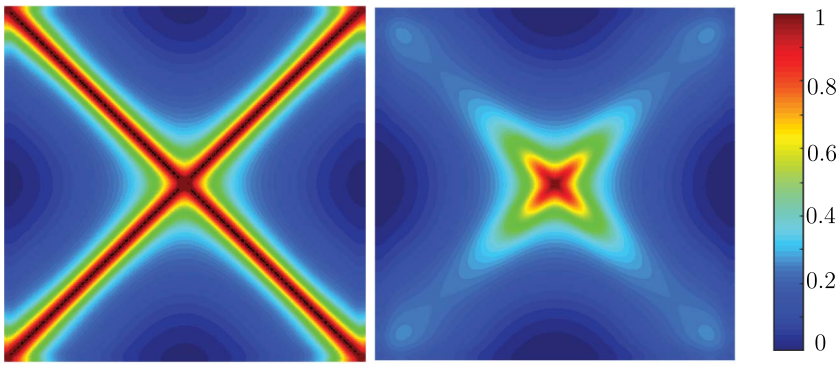

Fig. 15 Damage evolution profile corresponding to (*a*) hybrid model and (*b*) model with no T-C split at a given load step

Downloaded from http://asmedigitalcollection.asme.org/appliedmechanics/article-pdf/87/2/021002/6437224/jam_87_2_021002.pdf by Indian Institute of Technology Hyderabad user on 24 November 2022

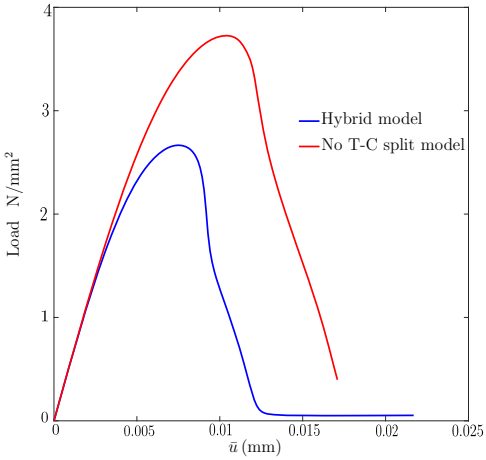

Fig. 16 Load versus deflection diagram

plate shows the softening behavior after a peak load of 0.11 N is reached.

7.2 Example 2: Thin Rectangular Plate Analysis. In this example, a thin rectangular plate of dimensions 2 mm(length) × 1 mm(width) and *a*/*h* equal to 100 (*a* being the length) is considered. SS-3 boundary conditions as shown in Fig. 8 are considered. A uniform mesh of 10,000 elements is considered, and the value of the length scale is fixed as 0.01 mm. A total load of 15 N is applied with initial λ value in the arc length method equal to 4×10^{-4}. The number of load steps used is 175.

Figure 13 shows the evolution of damage in the rectangular plate subjected to SS-3 boundary conditions. As it can be seen, the damage nucleates at the center of the plate and gradually propagates in the direction parallel to the length of the plate and then moves toward the corners. Figure 14 shows the load versus deflection graph.

7.3 Example 3: Comparison of Hybrid Model and the Model With No Tension-Compression Split. In this example, a square plate of dimensions 2 mm × 2 mm is considered for the analysis. SS-3 boundary conditions are applied and *a*/*h* is taken as 20. The value of the length scale is taken as 0.02 mm. A uniform mesh of 10,000 elements is used. A total load of 100 N is applied with an initial λ value in the arc length method equal to 4×10^{-4}. The number of load steps used are 175.

Figure 15 shows the damage profile associated with the hybrid and the model with no tension-compression split at the same value of the load step. It can be observed that the later model underpredicts the damage compared with the hybrid model. Figure 16 shows the load deflection graph. It is found that the model with no tension-compression split overpredicts the peak load.

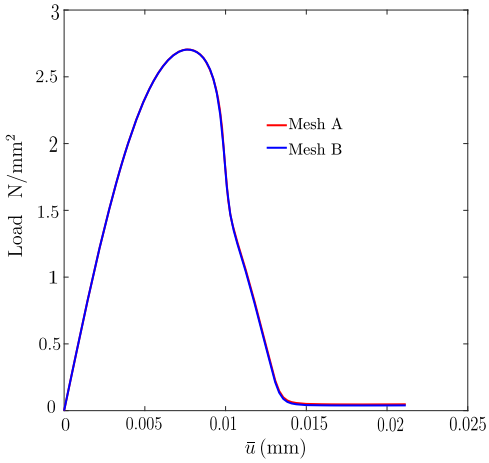

Fig. 18 Load versus deflection diagram of the plate subjected to SS-3 boundary conditions with different mesh sizes

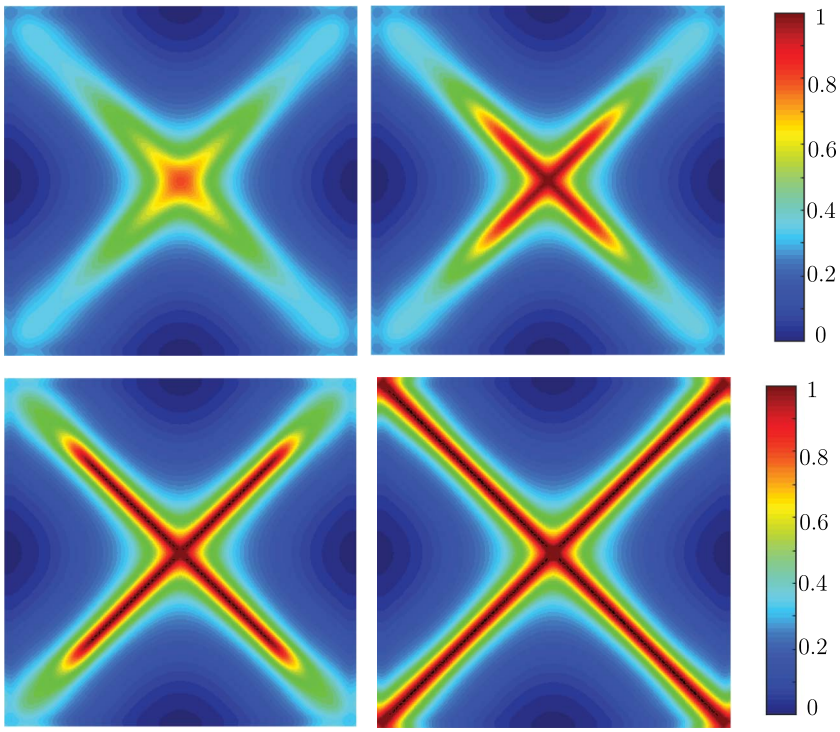

Fig. 17 Evolution of damage at different stages of loading in the plate subjected to SS-3 boundary conditions

Downloaded from http://asmedigitalcollection.asme.org/appliedmechanics/article-pdf/87/2/021002/6437224/jam_87_2_021002.pdf by Indian Institute of Technology Hyderabad user on 24 November 2022

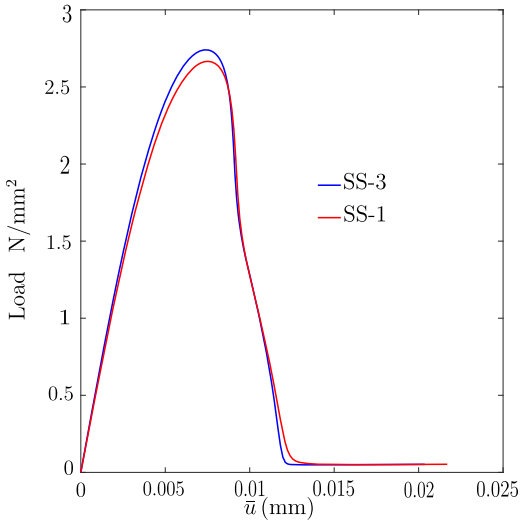

Fig. 19 Load versus deflection diagram

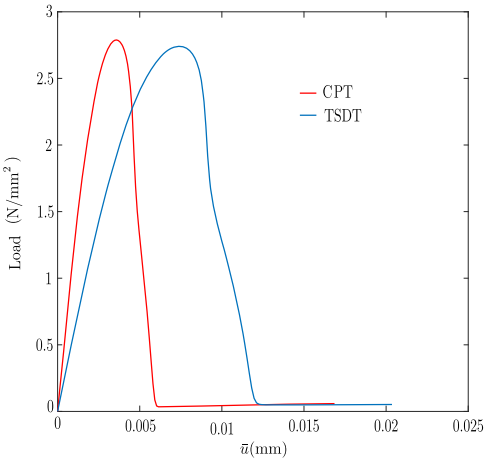

Fig. 20 Comparison of force-displacement response of CPT and TSDT for SS-3 boundary conditions

7.4 Example 4: Mesh Objectivity of the Phase Field Model. A square plate of dimensions 2 mm × 2 mm is considered. Two meshes of 10,000 and 40,000 elements are considered. The value of the length scale is chosen as 0.04 mm and a/h is taken as 20. A total load of 100 N is applied with an initial λ value in the arc length method equal to 8×10^{-4}. The number of load steps used is 100. The load-deflection diagram for the case of SS-3 boundary conditions corresponding to both meshes is shown in Fig. 18. A comparison of the load-deflection behavior between SS-1 and SS-3 boundary conditions is shown in Fig. 19. The comparison of force–displacement response (for the mesh size of 10,000 elements) associated with CPT and TSDT is shown in Fig. 20.

Figure 17 shows the evolution of damage in the plate at various load steps subjected to SS-3 boundary conditions for the mesh corresponding to 40,000 elements. It is seen that the damage initiates at

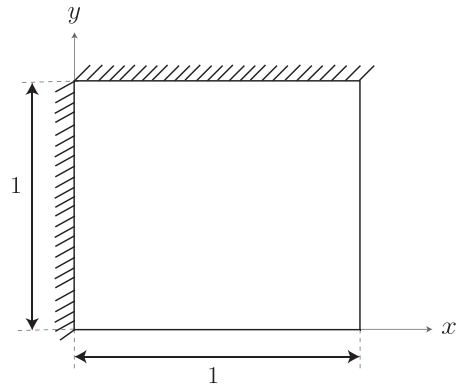

Fig. 21 Boundary conditions and dimensions of the plate

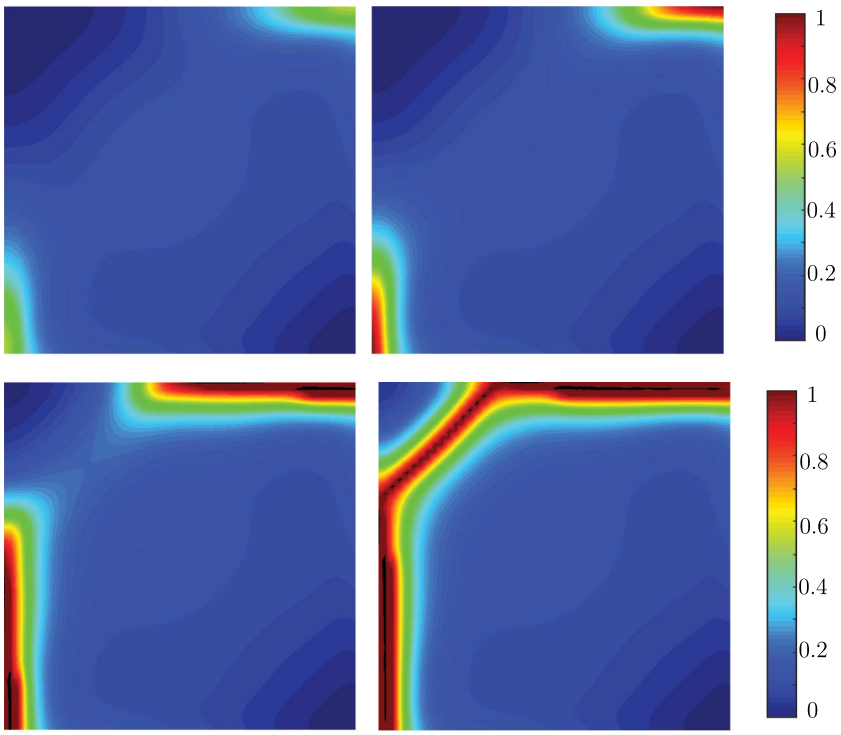

Fig. 22 Evolution of damage at different stages of loading

Downloaded from http://asmedigitalcollection.asme.org/appliedmechanics/article-pdf/87/2/021002/6437224/jam_87_2_021002.pdf by Indian Institute of Technology Hyderabad user on 24 November 2022

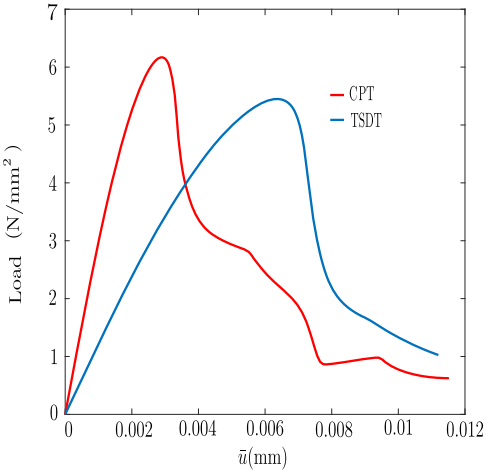

Fig. 23 Comparison of force–displacement response of CPT and TSDT

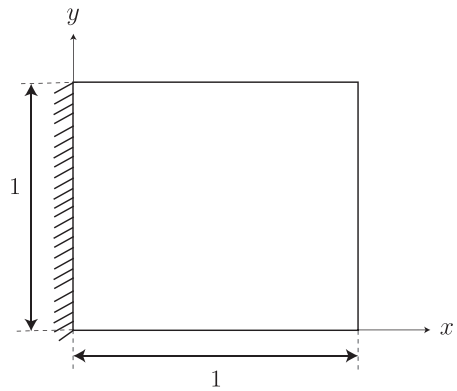

Fig. 24 Cantilever plate

the center of the plate and propagates toward the corners of the plate.

Figure 18 shows the load versus deflection diagram associated with two different meshes. Mesh A and Mesh B correspond to the discretization of 10,000 and 40,000 elements, respectively. It is clearly seen that the proposed phase-field model does not show mesh dependency in the load-deflection behavior unlike standard continuum damage models. Figure 19 shows the load deflection diagram corresponding to SS-1 and SS-3 boundary conditions. It is observed that SS-3 boundary conditions render the plate to carry a higher peak load compared with SS-1 boundary conditions. Figure 20 shows the load–displacement graph of PF models based on both CPT and TSDT. As it can be seen, there is a significant difference between the two graphs, especially after the peak load. The two theories predict almost the same value of peak load but at a different value of displacement.

7.5 Example 5. In this example, the boundary conditions as shown in Fig. 21 are considered for the analysis. The dimensions of the plate are taken as 1 mm × 1 mm. All the DOFs along the line $y = 1$ and $x = 0$ are constrained. The value of a/h and the length scale parameter are taken as 10, 0.04 mm respectively. A total load of 100 N is applied with an initial λ value in the arc length method equal to 3×10^{-4}. The number of load steps used is 400.

Figure 22 shows the damage evolution. It can be seen that the damage nucleates at the fixed edges of the plate and propagates toward the corner meeting the two fixed edges of the plate. Figure 23 shows the load versus normalized deflection diagram corresponding PF models based on CPT and TSDT. In this case, the peak load predicted by CPT significantly differs from that predicted by TSDT.

7.6 Example 6. In this example, we aim to understand the fracture patterns in a square cantilever plate of dimensions 1 mm × 1 mm as shown in Fig. 24. The value of a/h is taken as 10. A total load of 100 N is applied with an initial λ value in the arc length method equal to 5×10^{-4}. The number of load steps used is 100.

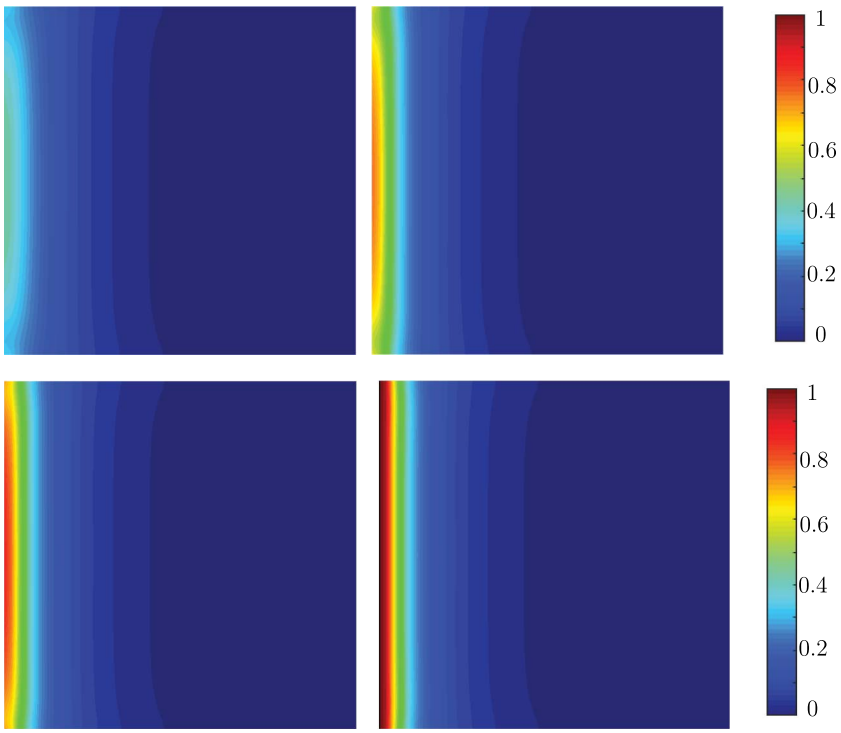

Fig. 25 Evolution of damage at different stages of loading in the cantilever plate

Downloaded from http://asmedigitalcollection.asme.org/appliedmechanics/article-pdf/87/2/021002/6437224/jam_87_2_021002.pdf by Indian Institute of Technology Hyderabad user on 24 November 2022

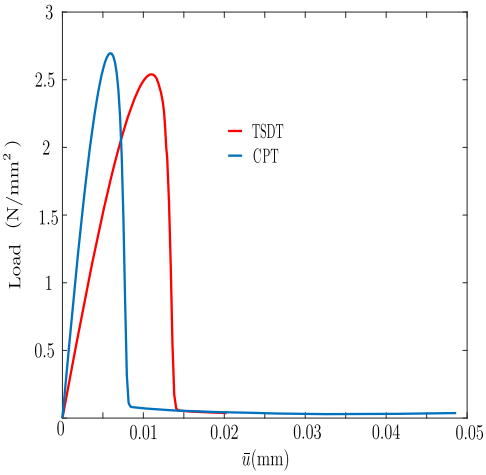

Fig. 26 Comparison of force–displacement response of CPT and TSDT for the cantilever plate

Figure 25 shows the damage evolution in the cantilever plate. As it can be seen, the damage initiates at the center of the fixed edge and propagates toward the corners of the fixed edge. Figure 26 shows the load-deflection graph for both CPT and TSDT phase field models. Similar to the previous example, CPT predicts the higher value of peak load compared with PF model based on TSDT.

8 Conclusions

A new phase-field model based on the hybrid formulation has been developed for the brittle fracture analysis of thick plates. Third-order shear deformation theory of Reddy has been employed to correctly capture the effect of shear deformation on the mechanical behavior of the plate. The elastic and the phase-field governing equations are derived based on the minimization of the free-energy functional that accounts for the shear deformation effects. The discretized weak forms of both the equations are developed using the finite element method. Staggered solution algorithm with arc length control has been used to find the evolution of damage. It is seen that the hybrid model significantly differs from the model with no tension-compression split of the strain energy, in predicting the peak load of the structure. This is because the history parameter is calculated based on the positive part of the strain energy in the hybrid formulation. The proposed model also shows the mesh objectivity in the post-peak regime. The difference in the mechanical response of PF models based on both CPT and TSDT has been shown for the case of thick plates and a significant difference between the two models is observed. In all the cases, CPT predicts a slightly higher value of peak load but at much lesser value of displacement compared with TSDT. This concludes the importance of choosing TSDT over CPT to analyze thick plates. Different numerical examples that are presented show the nucleation and propagation of the damage in the thick plate subjected to different boundary conditions. A parametric study has been conducted to illustrate the effect of boundary conditions, mesh size on the damage patterns, and load-deflection behavior.

References

[1] Griffith, A. A., 1921, "The Phenomena of Rupture and Flow in Solids," Philos. Trans. R. Soc. London, Ser. A, **221**(582–593), pp. 163–198.
[2] Marigo, J. J., Maurini, C., and Pham, K., 2016, "An Overview of the Modelling of Fracture by Gradient Damage Models," Meccanica, **51**(12), pp. 3107–3128.
[3] Dugdale, D. S., 1960, "Yielding of Steel Sheets Containing Slits," J. Mech. Phys. Solids, **8**(2), pp. 100–104.
[4] Barenblatt, G., 1962, "The Mathematical Theory of Equilibrium of Cracks in Brittle Fracture," Adv. Appl. Fract., **7**(1), pp. 55–129.
[5] Alfano, G., and Crisfield, M. A, 2001, "Finite Element Interface Models for the Delamination Analysis of Laminated Composites: Mechanical and Computational Issues," Int. J. Numer. Methods Eng., **50**(7), pp. 1701–1736.
[6] Jirásek, M., 2004, "Nonlocal Theories in Continuum Mechanics," Acta Polytech., **44**(5-6), pp. 16–34.
[7] de Borst, R., Sluys, L. J., and Mühlhaus, H. B., 1993, "Fundamental Issues in Finite Element Analysis of Localization of Deformation," Eng. Comput., **10**(2), pp. 99–121.
[8] Bažant, Z. P., and Pijaudier-Cabot, G., 1988, "Nonlocal Continuum Damage, Localization Instability and Convergence," ASME J. Appl. Mech., **55**(2), pp. 521–539.
[9] Peerlings, R. H. J., de Borst, R., and Brekelmans, W. A. M., 1996, "Gradient-Enhanced Damage for Quasi-Brittle Materials," Int. J. Numer. Methods Eng., **39**(39), pp. 3391–3403.
[10] Pijaudier-Cabot, G., and Burlion, N., 1996, "Damage and Localisation in Elastic Materials With Voids," Int. J. Mech. Cohesive Frict. Mater., **1**(2), pp. 129–144.
[11] Lorentz, E., 2017, "A Nonlocal Damage Model for Plain Concrete Consistent With Cohesive Fracture," Int. J. Fract., **207**(2), pp. 123–159.
[12] Areias, P., and Rabczuk, T., 2013, "Finite Strain Fracture of Plates and Shells With Configurational Forces and Edge Rotations," Int. J. Numer. Methods Eng., **94**(12), pp. 1099–1122.
[13] Borden, M. J., Hughes, T. J. R., Landis, C. M., Anvari, A., and Lee, I. J., 2016, "A Phase-Field Formulation for Fracture in Ductile Materials: Finite Deformation Balance Law Derivation, Plastic Degradation, and Stress Triaxiality Effects," Comput. Methods Appl. Mech. Eng., **312**(1), pp. 130–166.
[14] Wu, J. Y., and Nguyen, V. P., 2018, "A Length Scale Insensitive Phase Field Damage Model for Fracture," J. Mech. Phys. Solids, **119**(1), pp. 20–42.
[15] Teichtmeister, S., Kienle, D., Aldakheel, F., and Keip, M. A., 2017, "Phase Field Modelling of Fracture in Anisotropic Brittle Solids," Int. J. Non Linear Mech., **97**(1), pp. 1–21.
[16] Alessi, R., Ambati, M., Gerasimov, T., Vidoli, S., and De Lorenzis, L., 2018, "Comparison of Phase-Field Models of Fracture Coupled With Plasticity," Adv. Comput. Plast.-Linear Mech., **46**(1), pp. 1–21.
[17] Mandal, T. K., Nguyen, V. P., and Heidarpour, A., 2019, "Phase Field and Gradient Enhanced Damage Models for Quasi-Brittle Failure: A Numerical Comparative Study," Eng. Fract. Mech., **207**, pp. 48–67.
[18] Tanné, E., Li, T., Bourdin, B., Marigo, J. J., and Maurini, C., 2018, "Crack Nucleation in Variational Phase Field Models of Brittle Fracture," J. Mech. Phys. Solids, **110**(1), pp. 80–99.
[19] Pham, K. H., Ravi-Chandar, K., and Landis, C. M., 2017, "Experimental Validation of a Phase Field Model for Fracture," Int. J. Fract., **205**(1), pp. 83–101.
[20] Areias, P., Reinoso, J., Camanho, P. P., César de Sá, J., and Rabczuk, T., 2018, "Effective 2D and 3D Crack Propagation With Local Mesh Refinement and the Screened Poisson Equation," Eng. Fract. Mech., **189**, pp. 339–360.
[21] Msekh, M. A., Cuong, N. H., Zi, G., Areias, P., Zhuang, X., and Rabczuk, T., 2018, "Fracture Properties Prediction of Clay/epoxy Nano Composites with Interphase Zones Using a Phase Field Model," Eng. Fract. Mech., **188**, pp. 287–299.
[22] Feng, D. C., and Wu, J. Y., 2018, "Phase-Field Regularized Cohesive Zone Model (CZM) and Size Effect of Concrete," Eng. Fract. Mech., **197**, pp. 66–79.
[23] Wang, Z., and Poh, L. H., 2018, "A Homogenized Localizing Gradient Damage Model With Micro Inertia Effect," J. Mech. Phys. Solids, **116**, pp. 370–390.
[24] Francfort, G. A., and Marigo, J. J., 1998, "Revisiting Brittle Fracture As An Energy Minimization Problem," J. Mech. Phys. Solids, **46**(8), pp. 1319–1342.
[25] Bourdin, B., Francfort, G. A., and Marigo, J. J., 2000, "Numerical Experiments in Revisited Brittle Fracture," J. Mech. Phys. Solids, **48**(4), pp. 797–826.
[26] Ambrosio, L., and Tortorelli, V. M., 1990, "Approximation of Functional Depending on Jumps by Elliptic Functional Via T-Convergence," Commun. Pure Appl. Math., **43**(8), pp. 999–1036.
[27] Del Piero, G., Lancioni, G., and March, R., 2007, "A Variational Model for Fracture Mechanics: Numerical Experiments," J. Mech. Phys. Solids, **55**(12), pp. 2513–2537.
[28] Ambati, M., and De Lorenzis, L., 2016, "Phase-Field Modeling of Brittle and Ductile Fracture in Shells With Isogeometric NURBS-Based Solid-Shell Elements," Comput. Methods Appl. Mech. Eng., **312**, pp. 351–373.
[29] Miehe, C., Welschinger, F., and Hofacker, M., 2010, "Thermodynamically Consistent Phase-Field Models of Fracture: Variational Principles and Multi-Field FE Implementations," Int. J. Numer. Methods Eng., **83**(10), pp. 1273–1311.
[30] Ambati, M., Gerasimov, T., and De Lorenzis, L., 2015, "Phase-Field Modeling of Ductile Fracture," Comput. Mech., **55**(5), pp. 1017–1040.
[31] Miehe, C., Teichtmeister, S., and Aldakheel, F., 2016, "Phase-Field Modelling of Ductile Fracture: a Variational Gradient-Extended Plasticity-Damage Theory and Its Micromorphic Regularization," Philos. Trans. R. Soc. A, **374**(2066), pp. 1–18.
[32] Borden, M. J., Verhoosel, C. V., Scott, M. A., Hughes, T. J. R., and Landis, C. M., 2012, "A Phase-Field Description of Dynamic Brittle Fracture," Comput. Methods Appl. Mech. Eng., **217–220**, pp. 77–95.
[33] Hofacker, M., and Miehe, C., 2013, "A Phase Field Model of Dynamic Fracture: Robust Field Updates for the Analysis of Complex Crack Patterns," Int. J. Numer. Methods Eng., **93**(3), pp. 276–301.
[34] Ambati, M., Kruse, R., and De Lorenzis, L., 2016, "A Phase-Field Model for Ductile Fracture At Finite Strains and Its Experimental Verification," Comput. Mech., **57**(1), pp. 149–167.
[35] Lee, S., Wheeler, M. F., and Wick, T., 2016, "Pressure and Fluid-Driven Fracture Propagation in Porous Media Using An Adaptive Finite Element Phase Field Model," Comput. Methods Appl. Mech. Eng., **305**, pp. 111–132.
[36] Borden, M. J., Hughes, T. J. R., Landis, C. M., and Verhoosel, C. V., 2014, "A Higher-Order Phase-Field Model for Brittle Fracture: Formulation and Analysis

Downloaded from http://asmedigitalcollection.asme.org/appliedmechanics/article-pdf/87/2/021002/6437224/jam_87_2_021002.pdf by Indian Institute of Technology Hyderabad user on 24 November 2022

Within the Isogeometric Analysis Framework," Comput. Methods Appl. Mech. Eng., **273**, pp. 100–118.
[37] Rajagopal, A., Fischer, P., Kuhl, E., and Steinmann, P., 2010, "Natural Element Analysis of the Cahn-Hilliard Phase Field Model," Comput. Mech., **46**(3), pp. 471–493.
[38] Verhoosel, C. V., and de Borst, R., 2013, "A Phase-Field Model for Cohesive Fracture," Int. J. Numer. Methods Eng., **96**(1), pp. 43–62.
[39] Vignollet, J., May, S., de Borst, R., and Verhoosel, C. V., 2014, "Phase Field Models for Brittle and Cohesive Fracture," Meccanica, **49**(11), pp. 2587–2601.
[40] Alessi, R., Marigo, J. J., and Vidoli, S., 2014, "Gradient Damage Models Coupled With Plasticity and Nucleation of Cohesive Cracks," Arch. Ration. Mech. Anal., **214**(2), pp. 575–615.
[41] Geelen, R. J. M., Liu, Y., Hu, T., Tupek, M. R., and Dolbow, J. E., 2019, "A Phase-Field Formulation for Dynamic Cohesive Fracture," Mech. Mater., **348**, pp. 680–711.
[42] Hansen-Dörr, A. C., De Borst, R., Hennig, P., and Kästner, M., 2019, "Phase-Field Modelling of Interface Failure in Brittle Materials," Comput. Methods Appl. Mech. Eng., **346**, pp. 25–42.
[43] Paggi, M., and Reinoso, J., 2017, "Revisiting the Problem of a Crack Impinging on An Interface: A Modeling Framework for the Interaction Between the Phase Field Approach for Brittle Fracture and the Interface Cohesive Zone Model," Comput. Methods Appl. Mech. Eng., **321**, pp. 145–172.
[44] Zhang, P., Hu, X., Yang, S., and Yao, W., 2019, "Modelling Progressive Failure in Multi-Phase Materials Using a Phase Field Method," Eng. Fract. Mech., **209**, pp. 105–124.
[45] Reinoso, J., Arteiro, A., Paggi, M., and Camanho, P. P., 2017, "Strength Prediction of Notched Thin Ply Laminates Using Finite Fracture Mechanics and the Phase Field Approach," Compos. Sci. Technol., **150**, pp. 205–216.
[46] Bleyer, J., and Alessi, R., 2018, "Phase-Field Modeling of Anisotropic Brittle Fracture Including Several Damage Mechanisms," Comput. Methods Appl. Mech. Eng., **336**, pp. 213–236.
[47] Dhas, B., Masiur Rahaman, Md., Akella, K., Roy, D., and Reddy, J. N., 2017, "A Phase Field Damage Model for Orthotropic Materials and Delamination in Composites," ASME J. Appl. Mech., **85**(1), pp. 1–11.
[48] Sargado, J. M., Keilegavlen, E., Berre, I., and Nordbotten, J. M., 2018, "High-Accuracy Phase-Field Models for Brittle Fracture Based on a New Family of Degradation Functions," J. Mech. Phys. Solids, **111**, pp. 458–489.
[49] Amiri, F., Millán, D., Shen, Y., Rabczuk, T., and Arroyo, M., 2014, "Phase Field Modelling of Fracture in Linear Thin Shells," Theor. Appl. Fract. Mec., **69**, pp. 102–109.
[50] Kiendl, J., Ambati, M., De Lorenzis, L., Gomez, H., and Reali, A., 2016, "Phase-Field Description of Brittle Fracture in Plates and Shells," Comput. Methods Appl. Mech. Eng., **312**, pp. 374–394.
[51] Areias, P., Rabczuk, T., and Msekh, M. A., 2016, "Phase-Field Analysis of Finite Strain Plates and Shells Including Element Subdivision," Comput. Methods Appl. Mech. Eng., **312**, pp. 322–350.
[52] Reddy, J. N., 1984, "A Simple Higher-Order Theory for Laminated Plates," ASME J. Appl. Mech., **51**(4), pp. 745–752.
[53] Ambati, M., Gerasimov, T., and De Lorenzis, L., 2015, "A Review on Phase-Field Models of Brittle Fracture and a New Fast Hybrid Formulation," Comput. Mech., **55**(2), pp. 383–405.
[54] Miehe, C., Hofacker, M., and Welschinger, F., 2010, "A Phase Field Model for Rate-Independent Crack Propagation: Robust Algorithmic Implementation Based on Operator Splits," Comput. Methods Appl. Mech. Eng., **199**(45-48), pp. 2765–2778.
[55] Raghu, P., Rajagopal, A., and Reddy, J. N., 2018, "Nonlocal Nonlinear Finite Element Analysis of Composite Plates Using TSDT," Compos. Struct., **185**, pp. 38–50.
[56] Riks, E., 1979, "An Incremental Approach to the Solution of Snapping and Buckling Problems," Int. J. Solids Struct., **15**(7), pp. 529–551.
[57] Crisfield, M. A., 1981, "A Fast Incremental/Iterative Solution Procedure That Handles Snap-Through," Comput. Struct., **13**, pp. 55–62.

Downloaded from http://asmedigitalcollection.asme.org/appliedmechanics/article-pdf/87/2/021002/6437224/jam_87_2_021002.pdf by Indian Institute of Technology Hyderabad user on 24 November 2022